Available online at www.sciencedirect.com
ScienceDirect
Ceramics International 35 (2009) 3355–3364
CERAMICS INTERNATIONAL
www.elsevier.com/locate/ceramint

Synthesis, characterization and optical properties of $Mg(OH)_2$ micro-/nanostructure and its conversion to MgO

Latha Kumari [a], W.Z. Li [a,*], Charles H. Vannoy [b], Roger M. Leblanc [b], D.Z. Wang [c]

[a] *Department of Physics, Florida International University, Miami, FL 33199, USA*
[b] *Department of Chemistry, University of Miami, Coral Gables, FL 33124, USA*
[c] *Department of Physics, Boston College, Chestnut Hill, MA 02467, USA*

Received 16 April 2009; received in revised form 4 May 2009; accepted 27 May 2009
Available online 7 July 2009

Abstract

Magnesium hydroxide ($Mg(OH)_2$) micro- and nanostructures have been synthesized by a single step hydrothermal route. Surface morphology analysis reveals the formation of micro- and nanostructures with varying shape and size at different synthesis conditions. Structural investigations by X-ray diffraction (XRD) and transmission electron microscopy (TEM) confirm that the synthesized material is $Mg(OH)_2$ with hexagonal crystal structure. An optical band gap of 5.7 eV is determined for $Mg(OH)_2$ nanodisks from the UV–vis absorption spectrum. A broad emission band with maximum intensity at around 400 nm is observed in the photoluminescence (PL) spectra of $Mg(OH)_2$ nanodisks at room temperature depicting the violet emission, which can be attributed to the ionized oxygen vacancies in the material. Furthermore, $Mg(OH)_2$ has been converted to MgO by calcination at 450 °C. Optical studies of the MgO nanodisks have shown an optical band gap of 3.43 eV and a broadband PL emission in the UV region. $Mg(OH)_2$ and MgO nanostructures with wide-band gap and short-wavelength luminescence emission can serve as a better luminescent material for photonic applications.
© 2009 Elsevier Ltd and Techna Group S.r.l. All rights reserved.

Keywords: A. Powder: Chemical preparation; B. Electron Microscopy; C. Optical properties; D. MgO

1. Introduction

Recently, nanostructures of magnesium oxide (MgO) and hydroxide ($Mg(OH)_2$) have been extensively studied. Magnesium and its alloys possess unique properties such as low weight and non-toxicity. These properties are found advantageous for various devices in the fields of electronics, aerospace, automotive applications and biomedicine [1–3]. Magnesium oxide, a very important wide-band gap insulator, has been attracting much attention due to its application in catalysis [4], toxic waste remediation [5], as additives in refractory, paint, and superconductor products [6–8], and in steel manufacturing because of its high corrosion-resistant behavior [9]. Magnesium hydroxide (Brucite) is commonly used as the flame-retardant filler in composite materials due to its ability to undergo endothermic dehydration in fire conditions [10]. It has also been used as acidic waste neutralizer in environmental protection, papermaking industry, as a fertilizer additive [11–13], and as the most important precursor for the synthesis of magnesium oxide [14].

Recently, much attention has been paid to the synthesis of MgO and $Mg(OH)_2$ nanostructures. $Mg(OH)_2$ nanostructures with versatile morphological structures can be prepared by several methods, such as electrodeposition [15], sol–gel technique [16], precipitation [17], hydrothermal [18], solvothermal [19] and microwave assisted synthesis [20]. Several reports demonstrated that these structures can be converted into each other (i.e. $MgO \leftrightarrow Mg(OH)_2$) by either hydration [21] or dehydration [22] procedures. Generally, the final properties of the nanocrystals strongly depend on their shape, agglomeration state and preparation process. Hydrothermal route is one of the most extensively employed techniques in the synthesis of metal oxide nanostructures. The hydrothermal method has many advantages. For example, a highly homogeneous crystalline product can be obtained directly at a relatively lower reaction temperature; it favors a decrease in agglomeration between particles, narrow particles size distribution, phase homogeneity, uniform composition, high product purity and controlled

* Corresponding author. Tel.: +1 305 348 7257; fax: +1 305 348 6700.
E-mail address: Wenzhi.Li@fiu.edu (W.Z. Li).

0272-8842/$36.00 © 2009 Elsevier Ltd and Techna Group S.r.l. All rights reserved.
doi:10.1016/j.ceramint.2009.05.035

particle morphology [23]. In this work, we discuss the synthesis of various nano-/microstructures of $Mg(OH)_2$ by hydrothermal technique and its conversion to MgO. Structural analysis is performed on the micro-/nanostructures of $Mg(OH)_2$. Optical properties of $Mg(OH)_2$ and MgO nanostructures are also discussed.

2. Experimental

2.1. Synthesis of magnesium hydroxide nanostructures

$Mg(OH)_2$ nanostructures were synthesized by a single step hydrothermal route. The starting materials used for the synthesis are magnesium nitrate hexahydrate ($Mg(NO_3)_2{\cdot}6H_2O$) and sodium hydroxide (NaOH). All the chemicals were analytic grade reagents (Fisher Scientific) and used without further purification. Experimental details are as follows: 0.5 M of $Mg(NO_3)_2{\cdot}6H_2O$ and 5 M of NaOH solutions were prepared in distilled water. The NaOH solution was slowly added to the $Mg(NO_3)_2{\cdot}6H_2O$ solution under manual stirring. Then, the mixture was placed in an ultrasonicator bath for about 30 min to obtain homogeneous solution. Further, 10 mL of the above solution was loaded into a 20 mL Teflon-lined autoclave, which was then filled with 2 mL of absolute ethanol as buffering agent. Finally, the autoclave was sealed and maintained at different temperatures in the range between 180 and 250 °C for 3–72 h (hydrothermal treatment time, t_H). The autoclave was then allowed to cool down to room temperature naturally. The precipitates were filtered, washed with distilled water first to remove the soluble nitrates and then with ethanol to reduce the agglomeration, and later dried at 80 °C for 1 h. The white colored material that resulted was later used for various characterizations. $Mg(OH)_2$ micro-/nanoparticles were also synthesized at 200 °C for 24 h with the addition of 0.1 g of urea and 0.1 g of PEG 2000 along with 0.4 M of $Mg(NO_3)_2{\cdot}6H_2O$ and varying molar concentrations of NaOH (0.4–2.0 M).

2.2. $Mg(OH)_2$ to MgO conversion by calcination

Some of the as-synthesized $Mg(OH)_2$ samples (at 200 °C for 3, 12 and 48 h) were subjected to calcination in a muffle furnace in air. The samples were first heated to 250 °C and held at that temperature for 1 h, then at 350 °C for 2 h, and finally at 450 °C for 2 h. The temperature was increased very slowly to avoid the sudden collapse of the Brucite structure, as well as preserve the morphological features of the micro-/nanocrystalline $Mg(OH)_2$ in the final MgO materials. In the present work, we have approached two different methods for the conversion of $Mg(OH)_2$ to MgO: (1) systematic calcination of the as-prepared $Mg(OH)_2$ material at 250–450 °C and (2) TGA measurement in the temperature range of 50–1000 °C.

2.3. Characterization

Surface morphology analysis of the $Mg(OH)_2$ and MgO materials was performed by a field emission scanning electron microscope (SEM, JEOL JSM-6330F) operated at an accelerating voltage of 15 kV. Transmission electron microscopy (TEM) and high resolution TEM (HRTEM) images, and selected-area electron diffraction (SAED) patterns were obtained from a JEOL-2010F apparatus employing an accelerating voltage of 200 kV. Crystal structure analysis was carried out by employing an X-ray diffractometer (D-8 Bruker-AXS) equipped with a Cu Kα radiation source (λ = 1.5406 Å) and a two-dimensional area detector. A UV–vis spectrum was obtained from Perkin-Elmer Lambda 900 UV/Vis/NIR spectrometer, and the photoluminescence spectra were recorded from SPEX FluoroLog spectrofluorometer (Horiba, Jobin Yvon). For the spectroscopic analysis, nanomaterials were dispersed in NaOH solution at room temperature and taken into a quartz cell (1 cm optical path length). Thermal behavior of the $Mg(OH)_2$ micro-/nanostructures was studied through thermogravimetric analysis (TGA) data, which were collected with a TA instruments TGA 2950 apparatus under Ar flow (100 sccm), in the temperature range of 50–1000 °C. The heating rate was 25 °C/min from 50 to 250 °C with equilibrium at 250 °C, 10 °C/min from 250 to 400 °C with equilibrium at 400 °C and 25 °C/min from 400 to 1000 °C.

3. Results and discussion

3.1. Surface morphology of $Mg(OH)_2$

The surface morphology of $Mg(OH)_2$ micro-/nanostructures is analyzed from SEM images. The $Mg(OH)_2$ materials with various shapes and sizes, synthesized at different hydrothermal reaction conditions are listed in Table 1. Fig. 1 shows the SEM images of $Mg(OH)_2$ microparticles synthesized at temperatures of 180, 200, and 250 °C for 24 and 48 h, respectively. The $Mg(OH)_2$ product synthesized at 180 °C for 24 h shows wide range of size distribution from hexagonal nanodisks to microdisks, which vary from about 120 nm to 4 μm in width and 75–150 nm in thickness (Fig. 1(a)). As the synthesis time increased to 48 h (Fig. 1(b)), the surface morphology changes from micro-/nanodisks to polyhedrons, which have 14 faces. These polyhedrons also show a wide range of size distribution with varying widths of around 200 nm to 2.5 μm and thicknesses of 170 nm to ∼2 μm. At the hydrothermal treatment temperature of 200 °C, the $Mg(OH)_2$ particles still maintain polyhedron shape similar to the materials synthesized at 180 °C, but with a slight decrease in size. The polyhedrons produced at 200 °C for a hydrothermal reaction with duration of 24 h have widths of 250 nm to 2.3 μm and thicknesses of around 150 nm to 1.7 μm (Fig. 1(c)). On the other hand, the polyhedrons formed for the duration of 48 h are about 340 nm to 2.55 μm wide and 130 nm to 1.4 μm thick (Fig. 1(d)). At the highest synthesis temperature of 250 °C, the particles produced for 24 h have widths of 170 nm to 2.2 μm and thicknesses of around 125–760 nm (Fig. 1(e)). The particles at this synthesis condition have a large quantity of nanostructures rather than microstructures and also show a wide range of particle size distribution. $Mg(OH)_2$ material formed at 250 °C for 48 h are around 380 nm to 1.7 μm wide and 210 nm to

Table 1
Synthesis conditions of $Mg(OH)_2$ materials and the experimental data obtained from SEM, TEM and XRD analysis.

Sample	Temp (°C)	Time (h)	Morphology (from SEM)	Particle size (from TEM)	Crystallite size (nm, from XRD)		I_{001}/I_{101}	I_{001}/I_{110}
					(1 0 1)	(0 0 1)		
1	180	24	Microdisks	–	–	–	–	–
2	180	48	Polyhedrons	–	–	–	–	–
3	200	03	Microdisks*	~3 μm	28.9	44.1	2.03	9.48
4	200	12	Nanodisks*	35–150 nm	23.3	32.8	0.77	2.73
5	200	24	Polyhedrons	–	–	–	–	–
6	200	48	Polyhedrons*	~1 μm	27.7	41.4	0.99	4.4
7	250	24	Polyhedrons	–	–	–	–	–
8	250	48	Polyhedrons	–	–	–	–	–

* Presented in detail in Section 3.

1.1 μm thick (Fig. 1(f)). From the SEM analysis, it is observed that as the hydrothermal treatment temperature and reaction duration increases, the particle size distribution decreases. At the synthesis temperature of 200 °C, with an increase in the treatment time, the polyhedron thickness range and particle size distribution range decreases. The polyhedron width to thickness ratio is also very well maintained at 200 °C. Hence, the hydrothermal reaction temperature of 200 °C is best suited

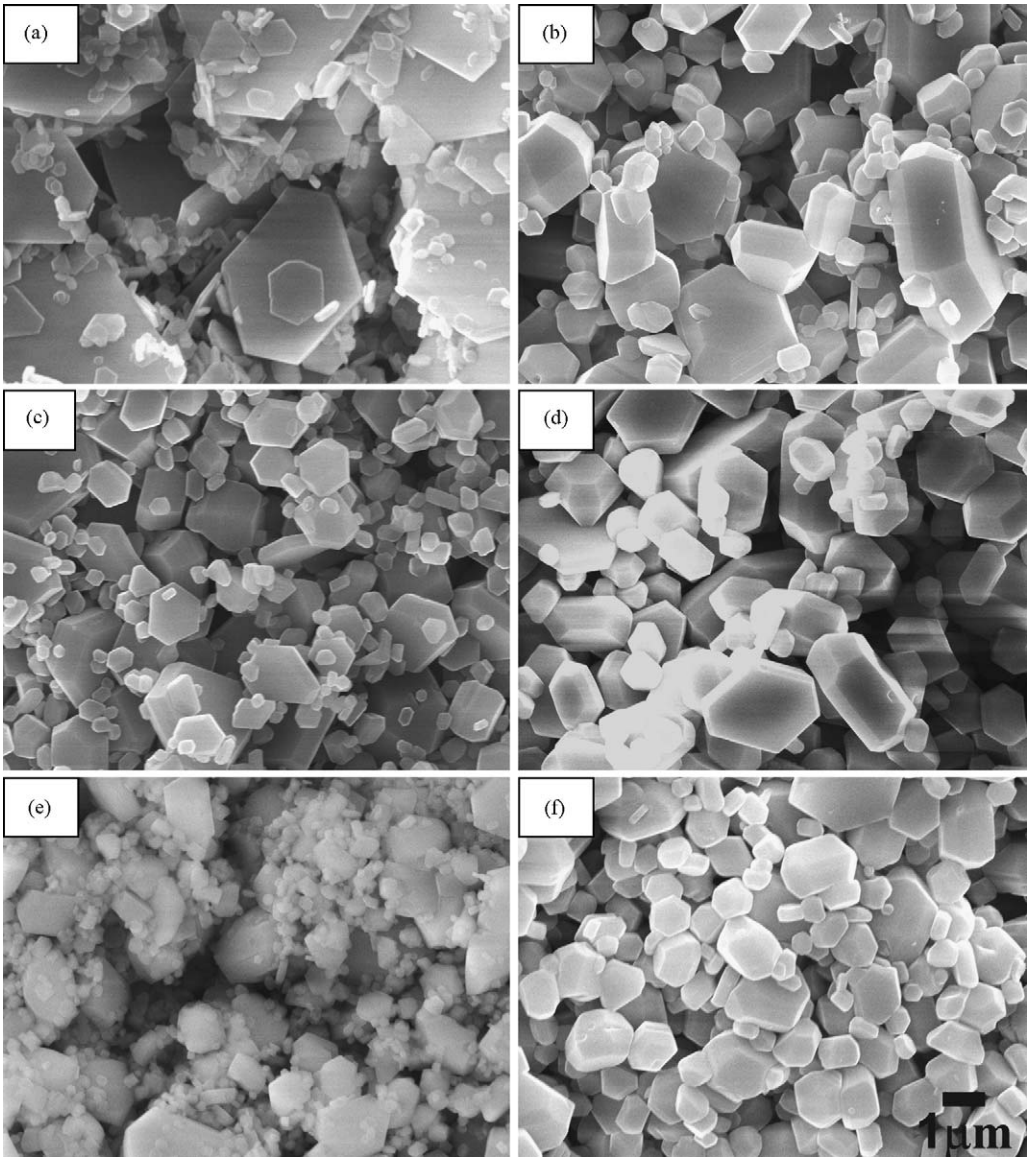

Fig. 1. SEM images of $Mg(OH)_2$ microstructures synthesized at different hydrothermal reaction conditions: (a) 180 °C, 24 h; (b) 180 °C, 48 h; (c) 200 °C, 24 h; (d) 200 °C, 48 h; (e) 250 °C, 24 h; and (f) 250 °C, 48 h. The scale bar is 1 μm.

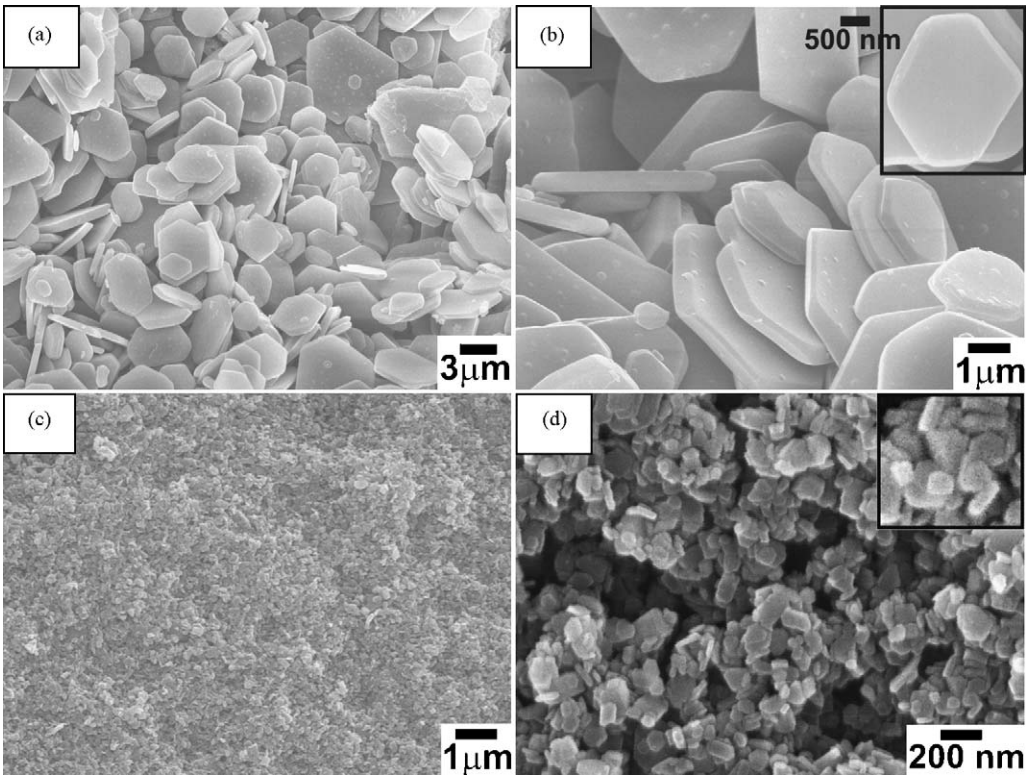

Fig. 2. SEM images of $Mg(OH)_2$ micro-/nanostructures produced at different hydrothermal synthesis conditions: (a) low-magnification, sample 3; (b) high-magnification, sample 3; Inset shows the plane view of the single microdisk; (c) low-magnification, sample 4 and (d) high-magnification, sample 4. Inset is the enlarged view of the nanodisks in sample 4.

for the synthesis of $Mg(OH)_2$ particles with better size distribution.

From various synthesis trials of $Mg(OH)_2$ material, it has been confirmed that 200 °C is the optimum temperature at which the effect of hydrothermal reaction duration can be very well observed. Hence, the $Mg(OH)_2$ material was also produced for low synthesis duration of 3 and 12 h to understand the effect of reaction time on the microstructure. Fig. 2 shows SEM

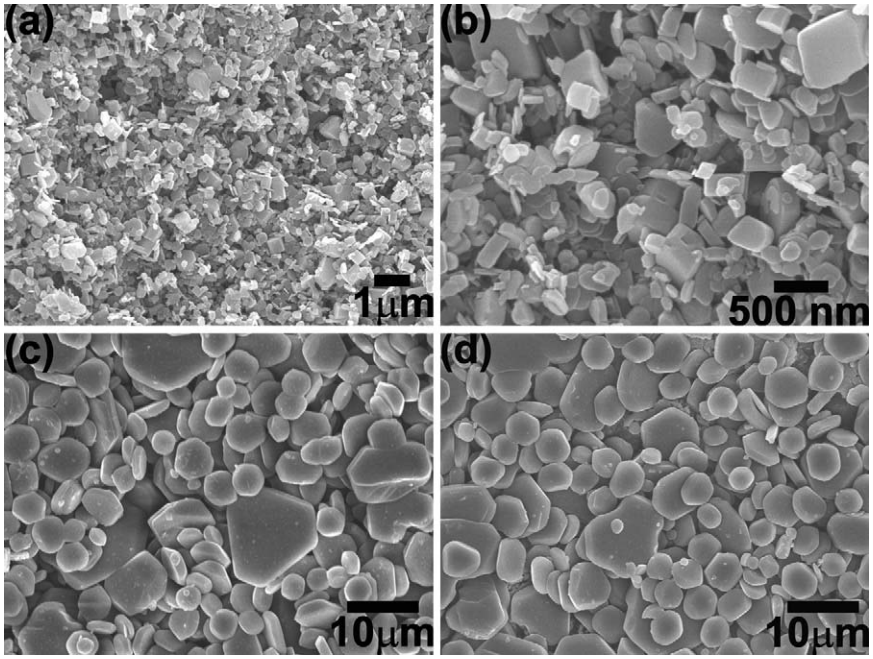

Fig. 3. SEM images of $Mg(OH)_2$ micro-/nanostructures synthesized at 200 °C for 24 h with addition of 0.1 g of urea, 0.1 g PEG and varying molar concentration of NaOH: (a) low-magnification, 0.4 M (b) high-magnification, 0.4 M, (c) 0.8 M and (d) 2.0 M.

images of $Mg(OH)_2$ particles synthesized at 200 °C for 3 and 12 h, respectively. Fig. 2(a) represents the low-magnification SEM image of the material synthesized for 3 h (sample 3), which shows the large scale view of the obtained product and Fig. 2(b) represents the high-magnification SEM image of the aforementioned sample. Sample 3 consists of hexagonal microdisks of varying width, from 1.0 to 3.5 μm and a thickness of about 500 nm. The inset of Fig. 2(b) shows a single hexagonal microdisk with a width of about 2.5 μm. The $Mg(OH)_2$ particle synthesized at 200 °C for 12 h (Fig. 2(c) and (d), sample 4) shows a contrast in surface morphology as compared to that of the samples formed at other synthesis conditions. Sample 4 depicts the formation of hexagonal nanodisks [24] of about 60–140 nm wide and around 45 nm thick. The overall hexagonal morphology of these disk-like particles is consistent with the hexagonal crystallographic characteristics of Brucite. The inset of Fig. 2(d) is a magnified view of the SEM image of sample 4 in Fig. 2(d). From the SEM images, it is evident that with an increase in the reaction time from 3 to 12 h, the $Mg(OH)_2$ particle sizes scale down from microdisks to nanodisks. Also, the samples synthesized for 12 h show a reduced particle size distribution as compared to the sample produced for 3 h. The thickness of the $Mg(OH)_2$ particles synthesized for 3 and 12 h are well controlled as compared to that of the samples synthesized for 24 and 48 h (Fig. 1(c) and (d)), which shows a wide range of thickness variation.

Previous works on the synthesis of various kinds of metal oxide nanostructures have utilized surfactants or structure directing agents to control the size and shape of the synthesized material. In the present work, the effect of the addition of urea and PEG on the size and shape of the $Mg(OH)_2$ particles has also been studied. Fig. 3 represents the SEM images of $Mg(OH)_2$ material synthesized at 200 °C for 24 h with a varying molar concentration of NaOH (0.4–2.0 M) and with the addition of urea and PEG. The low-magnification (Fig. 3(a)) and high-magnification (Fig. 3(b)) SEM images of the $Mg(OH)_2$ sample synthesized with 0.4 M NaOH shows nanoparticles of varying size, with widths of 70–780 nm and thicknesses of 30–450 nm. The increase in NaOH concentration to 0.8 M and then to 2.0 M produces $Mg(OH)_2$ microdisks. The material obtained with 0.8 M NaOH (Fig. 3(c)) consists of microdisks with very large widths, varying from 1.0 to 14 μm and having a thickness of about 1 μm. The $Mg(OH)_2$ sample synthesized with 2 M NaOH (Fig. 3(d)) also has microdisks that are about 1.0–15 μm wide and 1.7 μm thick. Hence, low molar concentration of NaOH is preferable for the synthesis of nanoparticles using surfactants. It is evident from the SEM analysis that the addition of urea and PEG are advantageous in controlling the nanoparticles' growth. The $Mg(OH)_2$ material synthesized at 200 °C for 24 h without PEG and urea reveal polyhedrons (microparticles) with large particle size variation (Fig. 1(c)), whereas the sample formed at similar synthesis conditions using PEG and urea reveal nanoparticles. Hence, optimized synthesis conditions can account for a controlled growth of nanoparticles.

3.2. X-ray diffraction analysis of $Mg(OH)_2$

The formation of particles from the hydrothermal route has some very interesting characteristics. Even a slight variation in the synthesis conditions will strongly affect the structural and morphological features of the resulting $Mg(OH)_2$ materials. The as-prepared $Mg(OH)_2$ samples which are in the form of small flakes are gently crushed for the XRD measurement. XRD patterns for $Mg(OH)_2$ micro-/nanoparticles synthesized at 200 °C for 3, 12 and 48 h (sample 3, 4 and 6, respectively) are shown in Fig. 4 (normalized intensity). All diffraction peaks in Fig. 4 can be indexed to the hexagonal Brucite structure of $Mg(OH)_2$ (JCPDS 7-239) with lattice constants of $a = 3.148$ Å and $c = 4.787$ Å. No peaks from other phases are observed, indicating a high purity of the synthesized material. The sharp peaks observed from the XRD pattern indicate that the $Mg(OH)_2$ particle has a sufficiently large grain size.

The mean crystallite size and the intensity ratio of reflections (0 0 1) to (1 0 1) and (1 1 0) for different samples (I_{001}/I_{101}, I_{001}/I_{110}) are listed in Table 1. From the XRD patterns, it is notable that the (0 0 1) peak became unusually strong and the relative intensity between (0 0 1) and (1 0 1) changed during the material synthesis duration. According to the standard file, the (1 0 1) peak should be the strongest one instead of (0 0 1) as noticed in our results, which reflects that the growth of crystals would be confined along the (0 0 1) direction. For sample 3, the intensity of the peak (0 0 1) is much larger than the (1 0 1) peak, whereas for sample 4, the intensity of the (0 0 1) peak is smaller than the (1 0 1) peak. On the other hand, sample 6 shows almost comparable intensities for the (0 0 1) and (1 0 1) peaks (Table 1). The value of the I_{001}/I_{101} ratio for sample 3, 4 and 6 are 2.03, 0.77 and 0.99, respectively, indicating the dominance of the (0 0 1) plane for sample 3 (Table 1). The diffraction peaks for sample 4 have a low intensity as compared to that of sample 3 and sample 6, indicating the reduced crystallinity in sample 4, which can be attributed to the porous nature of the synthesized material (Section 3.3). The slight peak broadening for sample 4 can be assigned to the small grain size

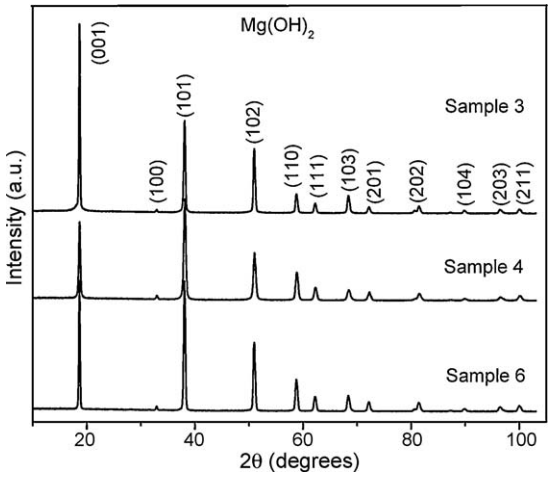

Fig. 4. XRD patterns of $Mg(OH)_2$ micro-/nanostructures synthesized at 200 °C for different hydrothermal treatment durations of 3, 12 and 48 h (sample 3, 4 and 6, respectively).

of $Mg(OH)_2$ particles. The crystallite size is determined by means of the Debye-Scherrer formula [25] based on the full width at half-maximum (FWHM). The estimated crystallite sizes for samples 3, 4 and 6 corresponding to the (0 0 1) plane are 44.1, 32.8 and 41.4 nm, respectively.

Moreover, from the intensities of the (0 0 1) and (1 1 0) reflection we can get a possible indication of the orientation of the particles. Usually in a hexagonal symmetry system, the normal direction of lamellar particles is (0 0 1). The (0 0 1) diffraction of sample 3 (microdisks) is stronger than that of sample 4 (nanodisks), and the (1 1 0) diffraction of sample 4 is stronger than that of sample 3. In addition, the I_{001}/I_{110} ratio for sample 4 and sample 6 are 2.7 and 4.4, respectively, while sample 3 exhibits a higher value of 9.5, indicating a more pronounced orientation of the microdisks towards the incident X-ray radiation. The crystallite sizes determined for samples 3, 4 and 6 corresponding to the (1 0 1) plane, are 28.9, 23.3 and 27.7 nm, respectively.

3.3. Structural analysis of $Mg(OH)_2$ by TEM

Fig. 5 illustrates the TEM images of sample 3 and sample 6. Fig. 5(a) represents the TEM image of sample 6 indicating that the clear hexagonal facets of the single polyhedron are about 900 nm wide. The HRTEM image of sample 6 acquired in the area indicated by the open box in Fig. 5(a) is shown in Fig. 5(b). The lattice fringes (Fig. 5(b)) are separated by a distance of 0.237 nm which can be attributed to the (1 0 1) plane of hexagonal phase of $Mg(OH)_2$. Fig. 5(c) is the TEM image of sample 3 depicting a single microdisk with a width around 3.25 μm and blunt hexagonal facets. The hexagonal spot patterns in the SAED (Fig. 5(d)) represent the [0 0 1] zone axis diffraction of the microdisks.

Fig. 6(a) illustrates the low-magnification TEM image of sample 4. The widths of these nanodisks are in the range of 35–150 nm. Fig. 6(b) shows an individual $Mg(OH)_2$ nanodisk with a hexagonal outline having a width of around 86 nm. The bumpy surface of the nanodisk indicates that it is composed of many primary building blocks (nanoparticles). The sixfold symmetry of the corresponding SAED pattern (Fig. 6(c)), which could be indexed to the [1 0 1] zone axis diffraction of the nanodisk, implies a better oriented arrangement of these primary blocks. From the HRTEM image in Fig. 6(d), slight disorientations in the fringe pattern are noticed; variations in the contrast reveal the presence of porosity and the internal interfaces between nanoparticles (mesopores as indicated by

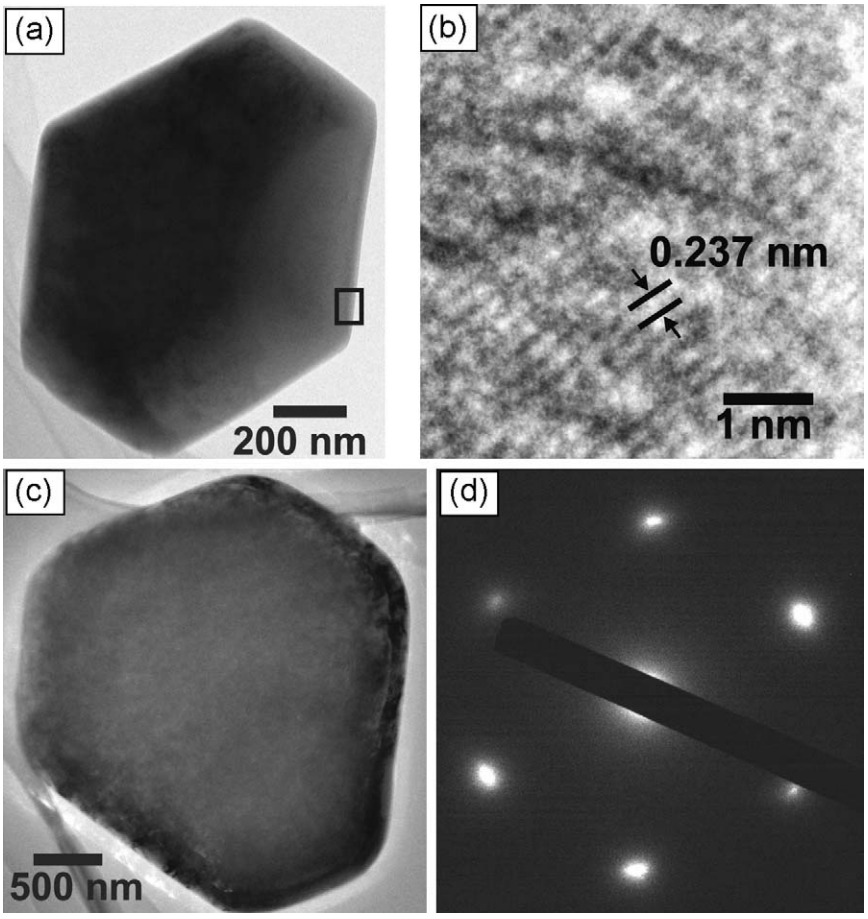

Fig. 5. TEM, HRTEM and SAED images of $Mg(OH)_2$ microstructures synthesized at 200 °C for different durations. (a) High-magnification TEM image of single polyhedron of sample 6 (48 h), (b) HRTEM image of sample 6 showing lattice fringes separated by 0.237 nm corresponding to the (1 0 1) plane, (c) High-magnification TEM image of single microdisk of sample 3 (3 h) and (d) SAED pattern of sample 3 representing the [0 0 1] zone axis diffraction of the microdisks.

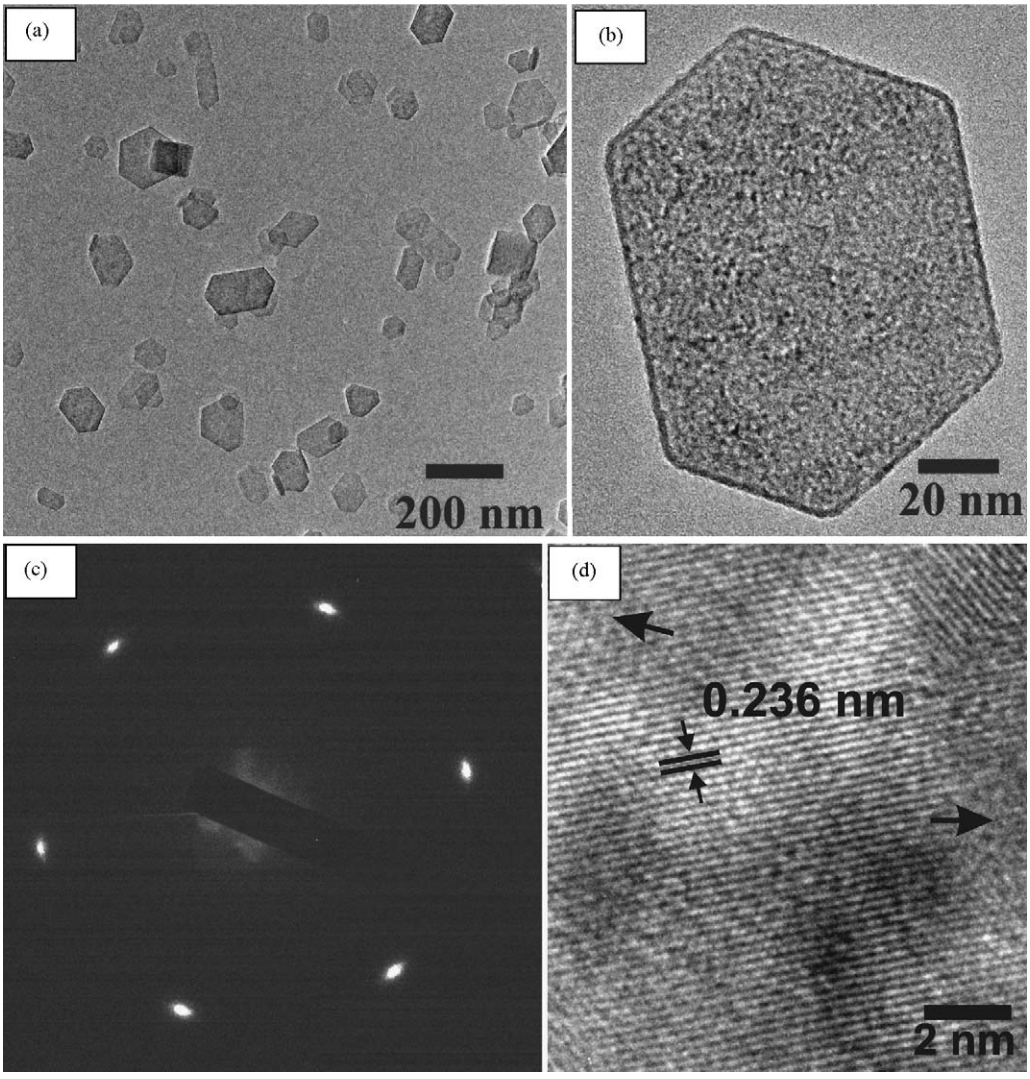

Fig. 6. (a) Low-magnification TEM image of nanodisks synthesized at 200 °C for 12 h (sample 4), (b) High-magnification TEM image of single nanodisk showing porous structure, (c) SAED pattern indicating the [0 0 1] zone axis diffraction of the nanodisks, and (d) HRTEM image of nanodisk with lattice fringes separated by 0.236 nm corresponding to the (1 0 1) plane of $Mg(OH)_2$.

the arrows) [24,26]. The porous nature of sample 4 is also confirmed by the reduced crystallinity as observed in the XRD pattern (Fig. 4). The lattice fringes in the HRTEM image (Fig. 6(d)) are separated by an interplanar distance of 0.236 nm representing the (1 0 1) plane of $Mg(OH)_2$.

3.4. UV–vis absorption and photoluminescence of $Mg(OH)_2$ nanodisks

Due to the nanostructure and appreciable particle size distribution of the $Mg(OH)_2$ nanodisks formed at 200 °C for 12 h, the optical properties of these nanodisks are studied in great detail. UV–vis absorption and photoluminescence spectra were obtained at room temperature for sample 4 consisting of $Mg(OH)_2$ nanodisks. Fig. 7(a) shows the UV–vis absorption spectrum for sample 4 in the wavelength range of 200–700 nm depicting the enhanced absorbance in the low (UV) wavelength region. The dependence of the absorption coefficient (α) on the photon energy ($h\gamma$) in the band-edge spectral region for a direct transition is given by the relation:

$$\alpha h\gamma = \text{Const}\,(h\gamma - E_g)^{1/2}$$

where α is the absorption coefficient, h is the Planck's constant, γ is the frequency of light and E_g is the band gap of the solid [27]. The inset of Fig. 7(a) shows $(\alpha h\gamma)^2$ vs. photon energy plot for the nanodisks and a direct energy band gap of 5.7 eV was determined from the plot. A Photoluminescence spectrum (Fig. 7(b)) was obtained for $Mg(OH)_2$ nanodisks (sample 4) in the wavelength range of 330–500 nm with an excitation wavelength of 290 nm. The PL emission spectrum of the nanodisks is fitted to four Gaussian peaks centered at 362, 387, 410 and 434 nm, which can be attributed to the transitions involving various Mg^{2+} states and oxygen states. It can be seen that the Gaussian curves fit the experimental data perfectly. The emission band with a peak maximum at around 434 nm is

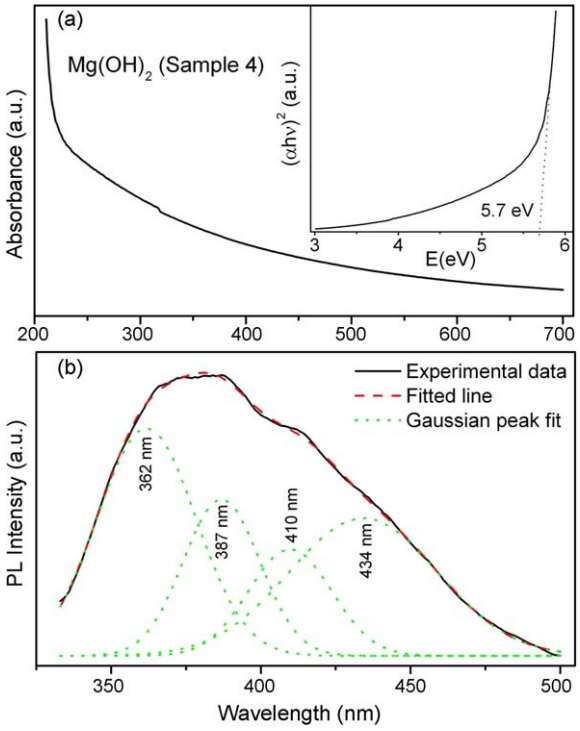

Fig. 7. (a) UV–vis absorption spectrum of nanodisks synthesized at 200 °C for 12 h (sample 4); Inset is the $(\alpha h\gamma)^2$ vs. photon energy plot and the calculated optical band gap is 5.7 eV and (b) photoluminescence spectrum of nanodisks recorded with a excitation wavelength of 290 nm, showing broad emission band and is fitted to four Gaussian peaks.

observed at the interface of UV and visible region which can be attributed to violet emission. The oxygen vacancies are expected to exist in the $Mg(OH)_2$ crystals, and these oxygen vacancies can induce the formation of defect states in the band gap region. In general, the PL emission spectra can be divided into two broad categories: the near-band-edge (NBE) emission and deep-level (DL) emissions. The UV emission in our sample can be associated with the NBE transitions. The broad emission band in the UV region can be attributed to the singly ionized oxygen vacancies in $Mg(OH)_2$ nanomaterials, and the emission is expected to result from the radiative recombination of a photo-generated hole with an electron occupying the oxygen vacancies. The two factors which favor the increase of the intensity of UV emission in nanostructures at room temperature are high crystal quality and quantum confinement. The wide-band gap $Mg(OH)_2$ nanostructures with short-wavelength PL emission can find application in light emitting devices.

3.5. Thermogravimetric analysis of $Mg(OH)_2$

The TGA measurement was carried out to analyze the thermal behavior and decomposition process of the as-synthesized $Mg(OH)_2$ materials. The TGA profiles for the $Mg(OH)_2$ samples synthesized at 200 °C for 3, 12 and 48 h (sample 3, 4 and 6, respectively) are as shown in Fig. 8. The marked weight loss is observed for sample 3, 4 and 6 in the temperature range of 280–450 °C, which can be attributed to the decomposition of $Mg(OH)_2$. The overall weight loss is

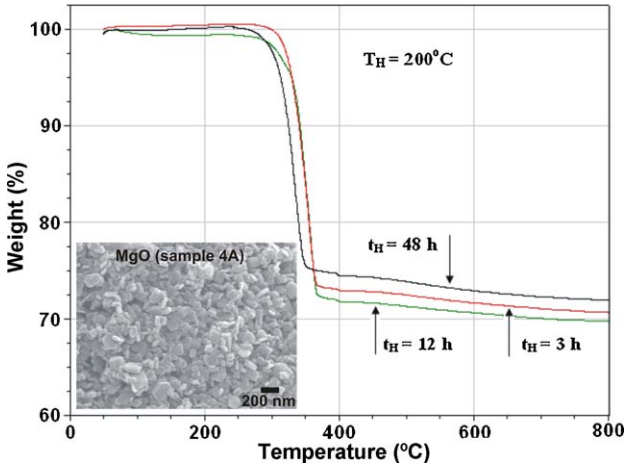

Fig. 8. TGA plots of $Mg(OH)_2$ micro-/nanostructures synthesized at 200 °C for 3, 12 and 48 h (sample 3, 4 and 6, respectively). Inset is the SEM image of MgO nanodisks (sample 4A).

determined to be 26.8, 27.5 and 23.8% for sample 3, 4 and 6, respectively (at 450 °C), which is slightly less than the reported weight loss of 31.04% for the complete decomposition of $Mg(OH)_2$ [28]. The difference in weight loss can be assigned to the incomplete decomposition reaction in this temperature range. The reported weight loss in the present work is in agreement with the previous reports on $Mg(OH)_2$ to MgO transformation [26,29]. The lower weight loss observed for sample 6 as compared to sample 3 and 4 can be attributed to the size and shape of the submicroparticles (polyhedrons). Sample 4 shows a higher value of weight loss owing to its nanostructure and porous nature. The incomplete decomposition of $Mg(OH)_2$ samples is also evident from the XRD analysis, which will be discussed later.

The MgO materials procured after the systematic calcination of the as-synthesized $Mg(OH)_2$ samples (sample 3, 4 and 6) in the temperature range of 250–450 °C are termed as sample 3A, 4A and 6A, respectively (see Section 2.2). The inset of Fig. 8 shows the SEM image of MgO nanodisks (sample 4A). From the SEM image, it can be concluded that the decomposition of $Mg(OH)_2$ to convert it to MgO does not induce any change in the surface morphology. The formation of nanodisks in $Mg(OH)_2$ (sample 4) is still maintained in MgO (sample 4A), but the nanodisks show slight variation in the dimensions. The nanodisks have widths of around 30–200 nm and thicknesses of about 15–30 nm. As compared to sample 4, the nanodisks in sample 4A show a slight increase in the particle size distribution and a reduced thickness, but preserve the structure of the particles.

3.6. Structure and properties of MgO

Fig. 9 shows the XRD patterns of the MgO samples, which are obtained by the decomposition of the $Mg(OH)_2$ materials. From the XRD patterns it is evident that even after systematic calcination of the $Mg(OH)_2$ (Brucite structure) material to convert it to MgO (Periclase structure), the weak and broad diffraction peaks corresponding to $Mg(OH)_2$ (indicated by #)

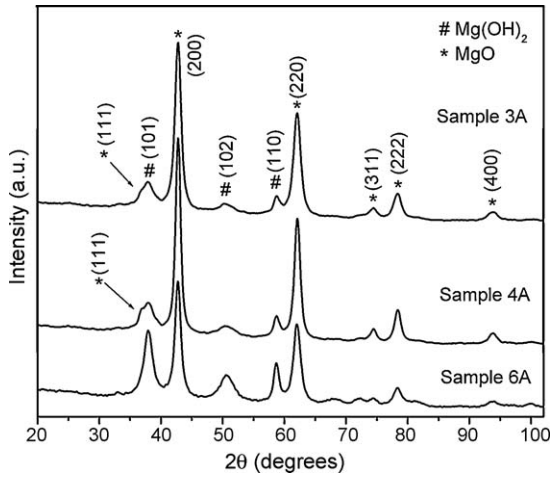

Fig. 9. XRD profiles of MgO samples (sample 3A, 4A and 6A). The diffraction peaks corresponding to $Mg(OH)_2$ and MgO are indicated by # and *, respectively.

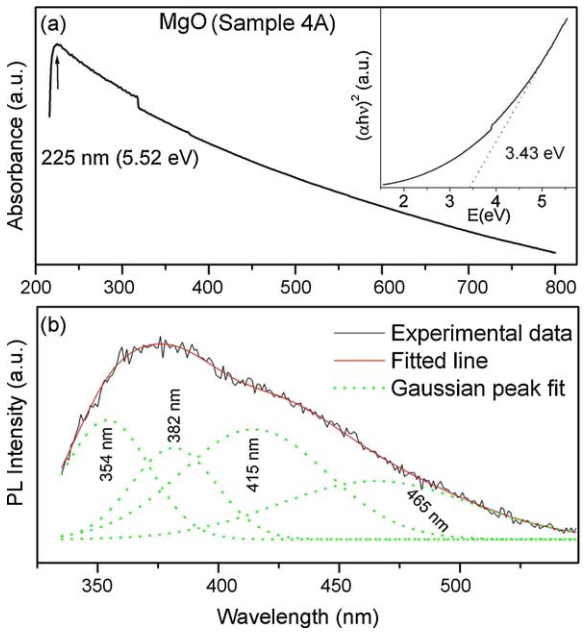

Fig. 10. (a) UV–vis absorption spectrum of MgO nanodisks (sample 4A); Inset is the $(\alpha h\gamma)^2$ vs. photon energy plot and the estimated optical band gap is 3.43 eV and (b) photoluminescence spectrum of MgO nanodisks showing broad emission band and is fitted to four Gaussian peaks.

still exist, which can be attributed to (1 0 1), (1 1 0) and (1 0 2) planes. The diffraction peaks (marked by *) other than the ones representing the $Mg(OH)_2$ can be indexed to a face-centered cubic phase of transformed MgO (JCPDS 87-0653) with a preferred orientation along the (2 0 0) direction. Sample 4A shows better crystallinity with sharp diffraction peaks, confirming the improved transformation of $Mg(OH)_2$ to MgO as compared to that of sample 3A and sample 6A. The XRD profile of sample 6A shows prominent peaks corresponding to (1 0 1), (1 1 0) and (1 0 2) reflections of $Mg(OH)_2$. A weak shoulder peak corresponding to (1 1 1) plane of MgO is observed for sample 3A and 4A, whereas there appears to be no shoulder for sample 6A. Hence, calcination even at 450 °C does not account for the complete decomposition of $Mg(OH)_2$ to form MgO.

Fig. 10 represents the UV–vis absorption and photoluminescence spectra for MgO nanodisks (sample 4A). The UV–vis absorption spectrum (Fig. 10(a)) was recorded in the wavelength range of 200–800 nm at room temperature. An absorption peak in the UV region with a wavelength of 225 nm (5.52 eV) can be associated to the band-to-band transition in the band gap region. A direct optical band gap of 3.43 eV was estimated for MgO nanodisks from the $(\alpha h\gamma)^2$ vs. Energy plot, in the inset of Fig. 10(a). In bulk form, MgO has a wide-band gap of around 7.3 eV. A large difference in the optical band gap of nanodisks as compared to their bulk counterpart can be attributed to the incomplete conversion of $Mg(OH)_2$ to MgO, as discussed in the TGA and XRD analysis. Fig. 10(b) shows a PL emission spectrum of the MgO nanodisks obtained in the 330–600 nm wavelength regions at room temperature. The observed broad emission band of MgO could be a superimposition of several peaks. Hence, the broad luminescence band of MgO nanodisks is fitted to four Gaussian peaks centered at around 354, 382, 415 and 465 nm. Most of these peaks exist in the UV region, and also at the interface of UV and visible region as compared to the previous works on MgO nanostructures [30,31] where the luminescence was observed mainly in the visible region. In the present work, during the evaporation and oxidation of the as-synthesized $Mg(OH)_2$ material to form MgO, oxygen vacancies are generated because of incomplete oxidation. Also, due to the porous nature of the MgO nanodisks and incomplete oxidation, the defects associated with oxygen vacancies, Mg vacancies and interstitials were generated, which would induce the formation of new defect levels in the band gap region of the MgO nanodisks and these defect states readily contribute to the luminescence [32,33]. The peaks corresponding to violet emission at 382 and 415 nm, and the blue emission peak at 465 nm are expected to originate from the defects in MgO, such as oxygen vacancies [30–33]. It has been reported [31] that MgO nanostructures possess more unique optical characteristics than those of the commercial MgO. Indeed, the PL bands observed for MgO nanodisks does not correspond to the band gap emission, but can be attributed to various structural defects. Previous work on high purity MgO crystals, suggested the luminescence bands at 390 and 530 nm, which were attributed to F (electron oxygen vacancies) and F^+ centers (ionized state of F center), respectively for an excitation wavelength of 248 nm [32,33]. The PL broad band of as-prepared porous MgO nanoplates [30] fitted to two Gaussian peaks centered at around 402 and 455 nm was expected to originate due to oxygen vacancies. The porous MgO nanodisks discussed in the present work also show similar features.

4. Conclusions

In summary, the $Mg(OH)_2$ micro-/nanostructures are synthesized by a hydrothermal route using magnesium salt as the starting material. Surface morphology analysis confirms the synthesis of various micro-/nanostructures of $Mg(OH)_2$ at different hydrothermal reaction conditions. XRD, HRTEM and SAED studies show that the synthesized $Mg(OH)_2$ material is of pure hexagonal phase. The present technique provides an

efficient route for the synthesis of $Mg(OH)_2$ microdisks, nanodisks and polyhedrons at 200 °C for 3, 12 and 48 h, respectively, that exhibit controlled morphology, high purity, uniform composition, and high crystallinity. The UV–vis spectrum for $Mg(OH)_2$ nanodisks shows an enhanced absorption intensity in the low wavelength region and an optical band gap of 5.7 eV is determined from the absorption spectra. The PL spectra show a broad emission band at the interface of UV and visible region (violet emission), which can be assigned to the ionized oxygen vacancies in the synthesized material. $Mg(OH)_2$ was decomposed at 450 °C to obtain MgO. MgO shows an enhanced optical absorption in the UV region and a broad luminescence band which originates from the defect states such as oxygen vacancies in MgO. The $Mg(OH)_2$ and MgO nanostructures with a wide-band gap and a short-wavelength luminescence emission can find potential application in optoelectronic sub-micron devices.

Acknowledgements

W.Z. Li acknowledges the support by the National Science Foundation under grant DMR-0548061. We would like to thank Mr. George P. Gomes and Mr. Kevin Hernandez, College of Engineering and Computing, Florida International University for their help with TGA measurement.

References

[1] K.U. Kainer, Magnesium Alloys and their Applications, Wiley-VCH, Weinheim, 2006.
[2] J.E. Gray, B. Luan, Protective coatings on magnesium and its alloys—a critical review, J. Alloys Compd. 336 (2002) 88–113.
[3] G. Song, D.St. John, Corrosion behaviour of magnesium in ethylene glycol, Corros. Sci. 46 (2004) 1381–1399.
[4] H. Tsuji, F. Yagi, H. Hattori, H. Kita, Self-condensation of n-butyraldehyde over solid base catalysts, J. Catal. 148 (1994) 759–770.
[5] A.N. Copp, Magnesia/magnesite, Bull. Am. Ceram. Soc. 74 (1995) 135–137.
[6] A. Bhargava, J.A. Alarco, I.D.R. Mackinnon, D. Page, A. Ilyushechkin, Synthesis and characterization of nanoscale magnesium oxide powders and their application in thick films of $Bi_2Sr_2CaCu_2O_8$, Mater. Lett. 34 (1998) 133–142.
[7] Y.S. Yuan, M.S. Wong, S.S. Wang, Solid-state processing and phase development of bulk $(MgO)_w$/BPSCCO high-temperature superconducting composite, J. Mater. Res. 11 (1996) 8–17.
[8] P.D. Yang, C.M. Lieber, Nanorod-superconductor composites: a pathway to materials with high critical current densities, Science 273 (1996) 1836–1840.
[9] B.M. Choudary, R.S. Mulukutla, K.J. Klabunde, Benzylation of aromatic compounds with different crystallites of MgO, J. Am. Chem. Soc. 125 (2003) 2020–2021.
[10] R.N. Rothon, Magnesium Hydroxide: New Products, Processes and Applications, Intertech, Portland, MA, 2000.
[11] J.L. Booster, A. Van Sandwijk, M.A. Reuter, Conversion of magnesium fluoride to magnesium hydroxide, Miner. Eng. 16 (2003) 273–281.
[12] J. Kang, P. Schwendeman, Comparison of the effects of $Mg(OH)_2$ and sucrose on the stability of bovine serum albumin encapsulated in injectable poly(D,L-lactide-co-glycolide) implants, Biomaterials 23 (2002) 239–245.
[13] R. Richards, W.F. Li, S. Decker, C. Davidson, O. Koper, V. Zaikovski, A. Volodin, T. Rieker, K.J. Klabunde, Consolidation of metal oxide nanocrystals. Reactive pellets with controllable pore structure that represent a new family of porous, inorganic materials, J. Am. Chem. Soc. 122 (2000) 4921–4925.
[14] Y. He, J. Wang, H. Deng, Q. Yin, J. Gong, Comparison of different methods to prepare MgO whiskers, Ceram. Int. 34 (2008) 1399–1403.
[15] G. Zou, W. Chen, R. Liu, Z. Xu, Morphology-tunable synthesis and characterizations of $Mg(OH)_2$ films via a cathodic electrochemical process, Mater. Chem. Phys. 107 (2008) 85–90.
[16] S. Utamapanya, K.J. Klabunde, J.R. Schlup, Nanoscale metal oxide particles/clusters as chemical reagents. Synthesis and properties of ultrahigh surface area magnesium hydroxide and magnesium oxide, Chem. Mater. 3 (1991) 175–181.
[17] J.P. Hsu, A. Nacu, Preparation of submicron-sized $Mg(OH)_2$ particles through precipitation, Colloids Surf. A 262 (2005) 220–231.
[18] Y.D. Li, M. Sui, Y. Ding, G. Zhang, J. Zhuang, C. Wang, Preparation of $Mg(OH)_2$ nanorods, Adv. Mater. 12 (2000) 818–821.
[19] W. Fan, S. Sun, L. You, G. Cao, X. Song, W. Zhang, H. Yu, Solvothermal synthesis of $Mg(OH)_2$ nanotubes using $Mg_{10}(OH)_{18}Cl_2{\cdot}5H_2O$ nanowires as precursors, Mater. Chem. 13 (2003) 3062–3065.
[20] H. Wu, M. Shao, J. Gu, X. Wei, Microwave-assisted synthesis of fibre-like $Mg(OH)_2$ nanoparticles in aqueous solution at room temperature, Mater. Lett. 58 (2004) 2166–2169.
[21] W. Feitknecht, H. Braun, Der mechanismus der hydratation von magnesiumoxid mit wasserdampf, Helv. Chim. Acta 50 (1967) 2040–2053.
[22] J. Green, Calcination of precipitated $Mg(OH)_2$ to active MgO in the production of refractory and chemical grade MgO, J. Mater. Sci. 18 (1983) 637–651.
[23] K. Byrappa, T. Adschiri, Hydrothermal technology for nanotechnology, Prog. Cryst. Growth Charact. Mater. 53 (2007) 117–166.
[24] B. Jia, L. Gao, Morphology transformation of nanoscale magnesium hydroxide: from nanosheets to nanodisks, J. Am. Ceram. Soc. 89 (2006) 3881–3884.
[25] H.P. Klug, L.E. Alexander, X-ray Diffraction Procedures, Wiley, New York, 1962.
[26] J.C. Yu, A. Xu, L. Zhang, R. Song, L. Wu, Synthesis and characterization of porous magnesium hydroxide and oxide nanoplates, J. Phys. Chem. B 108 (2004) 64–70.
[27] J.I. Pankove, Optical Processes in Semiconductors, Dover Publications, New York, 1971.
[28] J.C. Niepce, G. Watelle, Shear transformation in solid 1 → solid 2 + gas endothermic decompositions, J. Phys. Colloq. 38 (1977) 365–368.
[29] Y. Ding, G. Zhang, H. Wu, B. Hai, L. Wang, Y. Qian, Nanoscale magnesium hydroxide and magnesium oxide powders: control over size, shape, and structure via hydrothermal synthesis, Chem. Mater. 13 (2001) 435–440.
[30] H. Niu, Q. Yang, K. Tang, Y. Xie, A simple solution calcination route to porous MgO nanoplates, Microporous Mesoporous Mater. 96 (2006) 428–433.
[31] Y. Hao, G. Meng, C. Ye, X. Zhang, L. Zhang, Kinetics-driven growth of orthogonally branched single-crystalline magnesium oxide nanostructures, J. Phys. Chem. B 109 (2005) 11204–11208.
[32] G.H. Rosenblatt, M.W. Rowe, G.P. Williams Jr., R.T. Williams, Y. Chen, Luminescence of F and F^+ centers in magnesium oxide, Phys. Rev. B 39 (1989) 10309–10318.
[33] G.P. Summers, T.M. Wilson, B.T. Jeffries, H.T. Tohver, Y. Chen, M.M. Abraham, Luminescence from oxygen vacancies in MgO crystals thermochemically reduced at high temperatures, Phys. Rev. B 27 (1983) 1283–1291.